Experiments in Fluids (2018) 59:22
https://doi.org/10.1007/s00348-017-2464-1

RESEARCH ARTICLE

Accurate fluid force measurement based on control surface integration

David Lentink[1]

Received: 29 September 2017 / Revised: 15 November 2017 / Accepted: 18 November 2017

Abstract
Nonintrusive 3D fluid force measurements are still challenging to conduct accurately for freely moving animals, vehicles, and deforming objects. Two techniques, 3D particle image velocimetry (PIV) and a new technique, the aerodynamic force platform (AFP), address this. Both rely on the control volume integral for momentum; whereas PIV requires numerical integration of flow fields, the AFP performs the integration mechanically based on rigid walls that form the control surface. The accuracy of both PIV and AFP measurements based on the control surface integration is thought to hinge on determining the unsteady body force associated with the acceleration of the volume of displaced fluid. Here, I introduce a set of non-dimensional error ratios to show which fluid and body parameters make the error negligible. The unsteady body force is insignificant in all conditions where the average density of the body is much greater than the density of the fluid, e.g., in gas. Whenever a strongly deforming body experiences significant buoyancy and acceleration, the error is significant. Remarkably, this error can be entirely corrected for with an exact factor provided that the body has a sufficiently homogenous density or acceleration distribution, which is common in liquids. The correction factor for omitting the unsteady body force, $\rho_f/(\rho_b + \rho_f)$, depends only on the fluid, ρ_f, and body, ρ_b, density. Whereas these straightforward solutions work even at the liquid–gas interface in a significant number of cases, they do not work for generalized bodies undergoing buoyancy in combination with appreciable body density inhomogeneity, volume change (PIV), or volume rate-of-change (PIV and AFP). In these less common cases, the 3D body shape needs to be measured and resolved in time and space to estimate the unsteady body force. The analysis shows that accounting for the unsteady body force is straightforward to non-intrusively and accurately determine fluid force in most applications.

1 Introduction

To date, the most reliable technique for measuring the fluid mechanic force generated by vehicles and objects operating in fluids is based on mounting models to a load-cell to record the 3D force vector (Rae and Pope 1984). This technique works well for bodies that can be fixed to a sensor and where the inertia forces of the body can be subtracted or ignored such that they do not confound the force measurement (Lentink et al. 2015). Force has also been approximated using pressure measurements over the body and in the wake. Pressure taps can sample the pressure distribution over the surface of a wing or body to integrate the net pressure force time-resolved (Rae and Pope 1984). Similarly, wake rakes can be used to determine pressure loss in the wake of airfoils to estimate drag, provided the flow is attached and quasi-steady (Rae and Pope 1984).

For more complex force estimation in incompressible flow, including deformable bodies and freely flying animals (Spedding and Hedenstrom 2009; Tronchin et al. 2015; Gutierrez et al. 2016), the current state-of-the-art is based on measuring the unsteady flow field and integrating it using either a control volume (Noca et al. 1999; Unal et al. 1997; Poelma et al. 2006; Gemmell et al. 2015) or control surface (Mohebbian and Rival 2012; Rival and Van Oudheusden 2017) formulation of the Navier–Stokes equations—in combination with numerical pressure integration. Because pressure is calculated based on velocity, buoyancy contributions to fluid force are excluded. For accuracy, this approach relies on seeding the flow with tracers and using volumetric high-speed particle image velocimetry (PIV) to measure the 3D flow field in the control volume or over the control surface (Rival and Van Oudheusden 2017). Further, the velocity gradients have to be fully resolved in space and time so they can be integrated reliably. Although certain terms

✉ David Lentink
dlentink@stanford.edu

[1] Department of Mechanical Engineering, Stanford University, Stanford, USA

Published online: 29 December 2017

may be ignored for special cases, the exceptional resolution required for resolving turbulent flow in the imaging planes will remain a technological challenge for intermediate and high Reynolds number applications (Lentink et al. 2015). Another challenge is that the required data storage and post-processing of high-resolution flow fields is particularly computationally expensive for computing a simple three-component force time-series. An advantage of using the control surface formulation instead of the control volume approach is that data storage is less expensive; only measurements over the surface of the control volume need to be stored, rather than throughout the entire volume.

Recently, a new fluid mechanic force measurement technique was developed specifically for directly measuring the forces generated by freely moving animals in vivo, the aerodynamic force platform (AFP) (Lentink et al. 2015). This new technique mechanically integrates the control surface formulation of the Navier–Stokes equation time-resolved, regardless of the flow being turbulent. This has been verified and validated for quadcopters and birds in air (Lentink et al. 2015; Chin and Lentink 2017; Hightower et al. 2017). The experimental validations demonstrate the AFP's ability to directly measure the fluid force generated by freely moving animals, vehicles, and objects non-intrusively and accurately. A key benefit of the AFP is that the system integrates the control surface formulation time and space resolved regardless of the flow being turbulent (Lentink et al. 2015). The data storage requirements are minimal, because only the time-resolved six DOF ground reaction forces and moments of the platform's mechanical control surfaces need to be stored. Further, the computational requirements are straightforward; the ground reaction forces and moments that act on the mechanical control surfaces only need to be added vectorially. The walls can have windows for concurrent imaging, and the real-time force measurements can be used for closed-loop control manipulations. The method is non-intrusive, because animals, vehicles, and objects can freely move around in the control volume during recordings. This is also beneficial for fluid–structure interaction studies, because the force recordings are not confounded by inertial forces (which is a challenge when invertebrates, vehicles, and objects are mounted to a load-cell). The method is also non-invasive for animals, because animals are not exposed to laser light and all measurements take place behind the walls of the enclosure, so they do not interfere with the animal's behavior. Another benefit is that the AFP can be deployed both in the lab and in field settings, and can thus be applied very broadly (Hightower et al. 2017). Limitations such as wall interference effects are similar to wind tunnel test sections, resulting in a slight underestimation of flight power due to beneficial wall effects (reduced induced drag). However, the measured force is precise regardless, as the animal, vehicle or object would experience these beneficial effects due to the walls of any enclosure (Hightower et al. 2017). The mechanical design considerations of the AFP, in particular the aeroacoustic requirement of high frequency room modes in the control volume, and the structural requirement of high natural frequencies of the instrumented walls, have been described by Hightower et al. (Hightower et al. 2017). The high natural frequencies of the AFP should exceed the frequencies of interest to minimize amplitude and phase errors in unsteady force measurements.

The theoretical foundation of the AFP relies on the same control-surface integral derived and verified for calculating fluid force based on flow field measurements (Mohebbian and Rival 2012), in combination with the zero flow boundary condition on the (instrumented) walls of the AFP. Whereas these equations have been presented originally for deforming bodies (Wu et al. 2005), and have been implemented for rigid bodies in simulated flow fields (Mohebbian and Rival 2012), the evaluation of the unsteady body force term is still incomplete. A recent review noted that this term, introduced by the derivative-moment transformation to rewrite the volume integral for momentum flux into a surface integral, may be ignored when the volume of the body is thin (Rival and Van Oudheusden 2017). However, an error order-of-magnitude analysis to determine for which kinematics and body parameters the unsteady body force can be safely neglected in PIV and AFP measurements is missing. Further, a solution for experiments in which the unsteady body surface term cannot be neglected has yet to be proposed in the literature. Here, I will present a detailed error analysis to determine when the unsteady body force can be ignored without compromising accuracy, as well as a solution for determining the control surface integral when it cannot be ignored. Straightforward derivations result in a simple correction factor for determining the fluid force generated by bodies with homogenous density or acceleration distributions. Analogous derivations show the fluid force can also be measured at the liquid–gas interface in many cases. In other less common cases, the unsteady body force needs to be either estimated or measured, for which I propose experimental techniques. Direct applications of this analysis include measurement of the forces generated by freely moving vehicles, animals, and generalized 3D deforming bodies in fluids.

2 Control surface formulation

For an inertial frame of reference, the Reynolds transport theorem for conservation of momentum of an incompressible fluid in a deformable control volume is

$$\rho\frac{\mathrm{d}}{\mathrm{d}t}\iiint_V \mathbf{u}\ \mathrm{dV} + \rho\iint_{\partial V}\mathbf{u}[(\mathbf{u}-\mathbf{v})\cdot\mathbf{n}]\mathrm{d}S = -\iint_{\partial V} p\mathbf{n}\mathrm{d}S + \iint_{\partial V}\overline{\overline{\boldsymbol{\tau}}}\cdot\mathbf{n}\mathrm{d}S, \tag{1}$$

in which V is the control volume, ∂V the deformable surface of the volume, dV an infinitesimal control volume element, and dS an infinitesimal control surface element. Further, ρ is the density, t is time, $\mathbf{u}$ is the fluid velocity vector, $\mathbf{v}$ is the velocity vector of the control surface, $\mathbf{n}$ is the normal vector of the control surface, p is the fluid pressure, and $\overline{\overline{\boldsymbol{\tau}}}$ is the shear stress tensor (Wu et al. 2005). In this equation, we redefined the fluid pressure such that it includes the static pressure due to gravity, to account for buoyancy (further discussed in Sect. 3.5). The unsteady control volume integral can be recast into a control surface integral using the derivative-moment transformation (Wu et al. 2005) and Einstein notation (Mohebbian and Rival 2012) for brevity (in which x_i refers to the three Cartesian coordinate directions x, y, z for $i=1, 2, 3$),

$$\iiint_V \mathrm{u_i}\mathrm{d}V = \iiint_V \frac{\partial x_\mathrm{i}}{\partial x_\mathrm{j}}u_\mathrm{j}\mathrm{d}V = \iiint_V \frac{\partial}{\partial x_\mathrm{j}}(x_i u_j)\mathrm{dV} - \iiint_V x_i\frac{\partial u_\mathrm{j}}{\partial x_\mathrm{j}}dV = \iint_{\partial V} x_\mathrm{i}u_\mathrm{j}n_\mathrm{j}\mathrm{d}S. \tag{2}$$

Using the fact that $\partial x_i/\partial x_j$ corresponds to the identity tensor for $i=j$, that the divergence is zero for an incompressible fluid, $\partial u_j/\partial x_\mathrm{j}=0$, and applying Gauss' theorem, the control volume integral is transformed into a control surface formulation for the conservation of momentum,

$$\rho\frac{\mathrm{d}}{\mathrm{d}t}\iint_{\partial V}\mathbf{x}(\mathbf{u}\cdot\mathbf{n})\mathrm{d}S + \rho\iint_{\partial V}\mathbf{u}[(\mathbf{u}-\mathbf{v})\cdot\mathbf{n}]\mathrm{d}S = -\iint_{\partial V} p\mathbf{n}\mathrm{d}S + \iint_{\partial V}\overline{\overline{\boldsymbol{\tau}}}\cdot\mathbf{n}\mathrm{d}S. \tag{3}$$

Whereas this equation has been presented in different forms before (Wu et al. 2005; Mohebbian and Rival 2012; Rival and Van Oudheusden 2017), the difference here is that we will more carefully derive (1) how each surface integral term contributes to the net fluid force, and (2) when contributions may be neglected without sacrificing accuracy.

Using the control surface formulation, the calculation of the fluid force generated by an animal, vehicle, or generalized object immersed in the control volume requires integration of Eq. 3 over the entire control surface. To ensure the control surface, ∂V, is continuous (Fig. 1a), it has to combine the enclosing surface of the deforming body, $\partial B(t)$, the outer control surface, CS, and an infinitesimally thin tubular surface, $\partial b(t)$, that connects the body with the outer surface:

$$\partial V = CS \cup \partial B(t) \cup \partial b(t). \tag{4}$$

Because the connecting surface, ∂b(t), is infinitesimally thin, the unsteady, convective, pressure, and shear components are equal and opposite on opposing sides of the tubular surface, ∂b(t), which effectively forms a line cutting through the flow field. Therefore, the net integral contribution over ∂b(t) is zero, and the control surface integral (Eq. 3) for net fluid force $\mathbf{F}(t)$ on the body (Wu et al. 2005) simplifies to

$$\begin{aligned}\mathbf{F}(t) = &-\left(\iint_{\partial B} -p\mathbf{n}\mathrm{d}S + \iint_{\partial B}\overline{\overline{\boldsymbol{\tau}}}\cdot\mathbf{n}\mathrm{d}S\right)\\ &= -\iint_{CS} p\mathbf{n}\mathrm{d}S + \iint_{CS}\overline{\overline{\boldsymbol{\tau}}}\cdot\mathbf{n}\mathrm{d}S - \rho\frac{\mathrm{d}}{\mathrm{d}t}\iint_{CS}\mathbf{x}(\mathbf{u}\cdot\mathbf{n})\mathrm{d}S\\ &-\rho\iint_{CS}\mathbf{u}[(\mathbf{u}-\mathbf{v})\cdot\mathbf{n}]\,\mathrm{d}S - \rho\frac{\mathrm{d}}{\mathrm{d}t}\iint_{\partial B}\mathbf{x}(\mathbf{u}\cdot\mathbf{n})\mathrm{d}S,\end{aligned} \tag{5}$$

for particle image velocimetry (PIV; Fig. 1b) applications. The convective term in Eq. 5 vanished on the body surface because the difference between the velocity of the fluid touching the body and the velocity of the body surface must be zero due to the no-flow and no-slip boundary condition on walls, $\mathbf{u}-\mathbf{v}=\mathbf{0}$ for $\mathbf{x}\in\partial B(t)$. The control surface integral can be further simplified for the aerodynamic force platform (AFP; Fig. 1c) because the velocity boundary conditions on the outer surfaces are set to zero by the instrumented force plates. These plates form the outer control surface and mechanically integrate the pressure and shear stress distributions time and space resolved

$$\begin{aligned}\mathbf{F}(t) = &-\left(\iint_{\partial B} -p\mathbf{n}\mathrm{d}S + \iint_{\partial B}\overline{\overline{\boldsymbol{\tau}}}\cdot\mathbf{n}\mathrm{d}S\right)\\ &= -\iint_{\mathrm{CS}} p\mathbf{n}\mathrm{d}S + \iint_{\mathrm{CS}}\overline{\overline{\boldsymbol{\tau}}}\cdot\mathbf{n}\mathrm{d}S - \rho\frac{\mathrm{d}}{\mathrm{d}t}\iint_{\mathrm{CS}}\mathbf{x}(\mathbf{u}\cdot\mathbf{n})\mathrm{d}S.\end{aligned} \tag{6}$$

Whereas the net fluid force depends predominantly on the integrals over the outer control surface, both the PIV (Eq. 5) and AFP (Eq. 6) formulations share one additional term due to the unsteady motion of the control surface that encloses the body, $\partial B(t)$

$$\mathrm{UBF} = \rho\frac{\mathrm{d}}{\mathrm{d}t}\iint_{\partial B}\mathbf{x}(\mathbf{u}\cdot\mathbf{n})\mathrm{d}S. \tag{7}$$

This integral captures the force required to accelerate the fluid volume that was displaced by the body volume, B. The

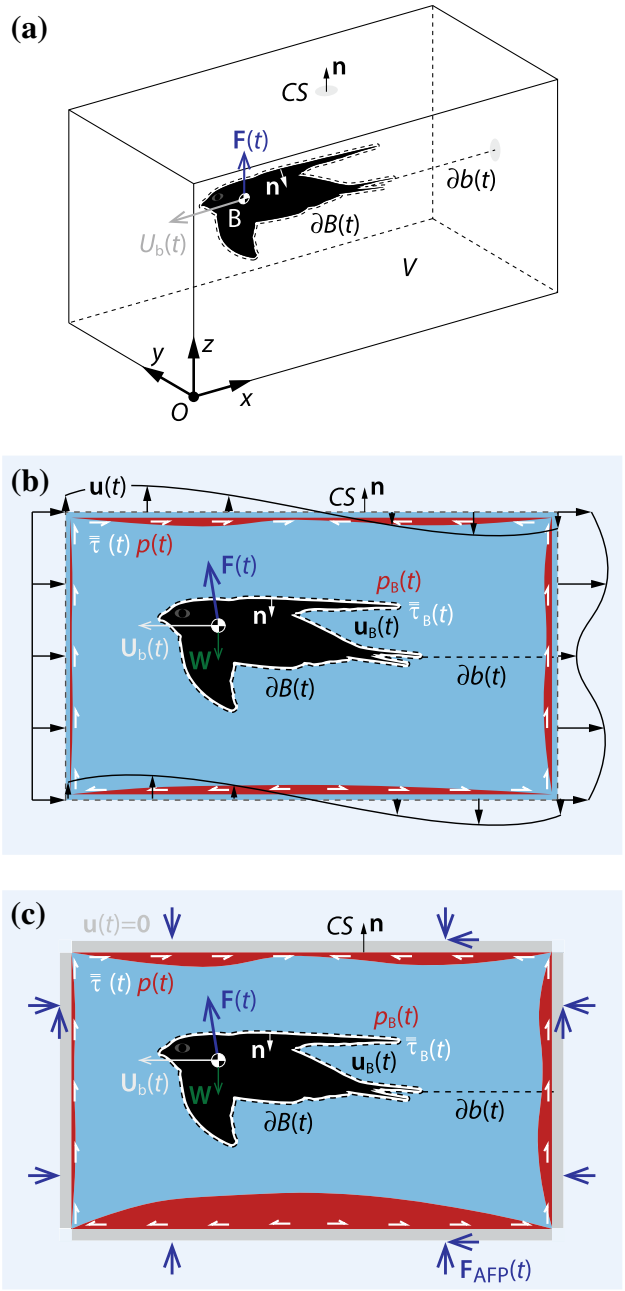

Fig. 1 Control surface formulation for an arbitrary deforming body moving through a fluid. **a** Definitions of the variables used in the formulation for control volume V, with the corresponding continuous control surface $\partial V = CS \cup \partial B(t) \cup \partial b(t)$, where CS is the outer control surface of the control volume, $\partial B(t)$ is the deforming body surface, $\partial b(t)$ is the infinitely thin tubular surface that connects CS with $\partial B(t)$, and $\mathbf{n}$ is the normal vector of the surface. The fluid force acting on the body at the center of gravity is $\mathbf{F}(t)$, $\mathbf{W}$ is the weight of the body, and $\mathbf{U}_b(t)$ is the velocity of the center of gravity of the body. The bird cartoon is enlarged for clarity and can be replaced with any deformable body of interest. **b** A sketch of the cross-section of the control surface typical for calculating force based on particle image velocimetry (PIV), corresponding to Eq. 5. To simplify the sketch, the velocity vectors on the outer control surface, CS, have been drawn along the direction of the surface normal, $\mathbf{n}$, whereas their directions are arbitrary in general. Further, to avoid clutter, the pressure, $p(t)$, shear tensor, $\overline{\overline{\tau}}$, and velocity distribution, $\mathbf{u}(t)$, are only shown on CS and not on $\partial B(t)$ and $\partial b(t)$. The subscript "B" refers to body. **c** A sketch of the cross-section of the control surface typical for measuring the force with an aerodynamic force platform (AFP), corresponding to Eq. 6. The control surface CS is physically represented by walls that have a no-flow boundary condition $\mathbf{u}(\mathbf{x} \in \mathrm{CS}, t) = \mathbf{0}$. The walls are made out of instrumented force plates that mechanically integrate the time-dependent fluid pressure and shear stress distributions over their surface, which is transferred to load cells that record components of the integral as $\mathbf{F}_{\mathrm{AFP}}(t)$. For details see (Lentink et al. 2015; Hightower et al. 2017; Chin and Lentink 2017). Both the PIV and AFP control surfaces are submerged in a larger volume of fluid (light blue), which is static around the AFP

calculation of this unsteady body force (UBF) is analogous to applying Archimedes principle for calculating buoyancy of a body in a static fluid undergoing gravity. Finally, the surface formulation can be rewritten into volumetric form using Gauss theorem (Saffman 1992; Rival and Van Oudheusden 2017; DeVoria et al. 2014)

$$\mathrm{UBF} = \rho \frac{\mathrm{d}}{\mathrm{d}t} \iiint_B \mathbf{u} \mathrm{d}V. \tag{8}$$

Rival and Van Oudheusden (2017) used this formulation to conclude that the unsteady body force vanishes when the body is sufficiently thin. However, it is unclear in which applications the unsteady body force can be neglected more generally, and how it can be measured when it is significant.

3 Results and discussion

To evaluate the unsteady body force in fluid force measurements, we follow a six-tiered approach. First, we perform an order-of-magnitude analysis to determine for which fluid and body density combinations the unsteady body force can be neglected and find it is negligible for all non-buoyant bodies. Second, we analyze the error for buoyant bodies with constant volume to determine for which combinations of body motions, shapes and densities the unsteady body force can be neglected. Third, we derive a correction factor to accurately determine the fluid force for constant-volume bodies experiencing buoyancy. Fourth, we approximate the fluid force for constant-volume bodies that dynamically deform at the liquid–gas interface. Fifth, we determine under which conditions the unsteady body force cannot be ignored for buoyant bodies due to variation in body density and volume over time. Finally, we discuss techniques to measure the unsteady body force for a subclass of buoyant bodies for which it cannot be neglected in PIV- and AFP-based force measurements.

To objectively define when the error in the fluid force measurement, F_{error}, can be neglected, we compare the error to the weight of the vehicle, animal, or object, W. The fluid force error fraction, $\varepsilon_{\text{F}} = F_{\text{error}}/W$, is the desired experimental error level, in which ε_{F} compares the error in the fluid force measurement to body weight. Based on the current state-of-the-art in non-intrusive fluid force measurement systems in engineering (Lentink et al. 2015), we set $\mathcal{O}(\varepsilon_{\text{F}}) \leqslant \varepsilon$ with $\mathcal{O}(\varepsilon) \leqslant 0.01$, in which ϵ represents the non-dimensional error fraction required for the experiment to be accurate. However, we also note that based on the current animal biomechanics literature $\mathcal{O}(\varepsilon) \leqslant 0.1$ may still be acceptable (Dickinson et al. 1999; Gutierrez et al. 2016; Poelma et al. 2006) whenever answering a biological question does not require higher accuracy.

3.1 Small fluid-body density ratios diminish force error

First, we consider animals (e.g., insects, bats and birds), vehicles (e.g., airplanes) and objects (e.g., fans and wind turbines) operating in fluids that have a much lower density than their average (body) density. The magnitude of the unsteady body force is proportional to the density of the fluid. To determine how it compares to the net force that acts on the vehicle, animal, or object, we apply Newton's second law of motion to relate it to the net body acceleration, $\mathbf{a}_{\text{b}}$. Integrating the generalized form of Newton's second law for the deforming body (Meriam and Kraige 1993), which we consider as a system of infinitesimal connected particles with an associated acceleration and mass field, we find

$$\mathbf{F}(t) - \mathbf{W} = -\left(\iint_{\partial B} -p\mathbf{n}\mathrm{d}S + \iint_{\partial B} \overline{\overline{\boldsymbol{\tau}}} \cdot \mathbf{n}\mathrm{d}S \right) - \mathbf{W} = \rho_{\text{b}} V_{\text{b}} \bar{\mathbf{a}}_{\text{b}}, \tag{9}$$

in which the net fluid force on the body, $\mathbf{F}(t)$, minus the weight of the body, $\mathbf{W}$, is equal to the product of body density, ρ_{b}, volume, V_{b}, and the body mass-averaged body acceleration, $\bar{\mathbf{a}}_{\text{b}}$, which acts at the center of mass of the body. If the body experiences significant buoyancy, this will contribute to balancing body weight via the static pressure contribution over the body surface. Whereas this static pressure contribution cannot be determined with PIV, the AFP can measure it if it is tared before the body enters the control volume and changes the static pressure distribution over the control surface. Next, we perform an analysis to estimate the order of magnitude of the unsteady body force term (Eq. 8)

$$\mathcal{O}\left(\rho_{\text{f}} \frac{\mathrm{d}}{\mathrm{d}t} \iiint_{B} \mathbf{u}\mathrm{d}V \right) = \rho_{\text{f}} V_{\text{b}} a_{\text{b}} \quad \left(\text{or} \quad \rho_{\text{f}} \dot{V}_{\text{b}} U_{\text{b}} \right), \tag{10}$$

which is proportional to fluid density, ρ_{f}, the volume of the body, V_{b}, and the magnitude of the body acceleration, a_{b}. Between parentheses we also present the magnitude for the case when body deformation dominates average body acceleration, in which $\dot{V}_{\text{b}}$ is the average rate of body volume change and U_{b} is the average body velocity. Here, we focus on cases in which $\mathcal{O}\left(V_{\text{b}} a_{\text{b}} / \dot{V}_{\text{b}} U_{\text{b}}\right) > 1$, because those are representative for most animals, vehicles and a large number of deforming objects, which all approximately have a body with constant volume, $\dot{V}_{\text{b}} = 0$. We quantify the integration error due to omitting the unsteady body force for arbitrary bodies that have a relatively constant volume by taking the outcome of Eq. 10 and comparing it to the order of magnitude of Eq. 9,

$$\varepsilon_{\rho} \equiv \frac{\rho_{\text{f}} V_{\text{b}} a_{\text{b}}}{\rho_{\text{b}} V_{\text{b}} a_{\text{b}}} = \rho_{\text{f}} / \rho_{\text{b}}. \tag{11}$$

This ratio shows that it is safe to neglect the unsteady body force integral (Eq. 7, 8) in any case in which the average body density is much larger than the fluid density. Most animals, vehicles, and objects in air have a density similar to or greater than water, which is about 800 times denser than air at sea level, corresponding to $\varepsilon_{\rho} \approx 0.001$, which reduces with altitude. More careful evaluation of the unsteady body force integral is required, however, for vehicles and objects submerged in gas that are near neutrally buoyant $\left(\varepsilon_{\rho} \approx 1\right)$ or buoyant $\left(\varepsilon_{\rho} > 1\right)$. Furthermore, for animals, vehicles, and objects submerged in liquids, the average body density will likely be on par with the fluid $\left(\varepsilon_{\rho} \approx 1\right)$. In general, buoyancy can result in a significant error whenever $\mathcal{O}\left(\varepsilon_{\rho}\right) > \mathcal{O}(\varepsilon)$, which requires a more careful analysis to determine when it can be neglected or should be corrected for.

3.2 Error analysis for buoyant bodies with constant volume

Now we focus on buoyant bodies with approximately constant volume such as animals (e.g., plankton, fish, swimming mammals), vehicles (e.g., submarines, zeppelins) and objects (e.g., balloons). Considering that the unsteady body force integral is expected to be of importance for animals, vehicles, and deforming objects that experience buoyancy, $\mathcal{O}\left(\varepsilon_{\rho}\right) > \mathcal{O}(\varepsilon)$, we will evaluate kinematics and shape parameters to determine when it can still be neglected safely.

First, we consider arbitrary buoyant bodies that do not accelerate. For this case, we find that any constant velocity distribution over the body surface will result in a net-zero unsteady body force integral (Eq. 8),

$$\rho_{\text{f}} \frac{\partial}{\partial t} \iiint_{B} \mathbf{u}\mathrm{d}V = \mathbf{0}. \tag{12}$$

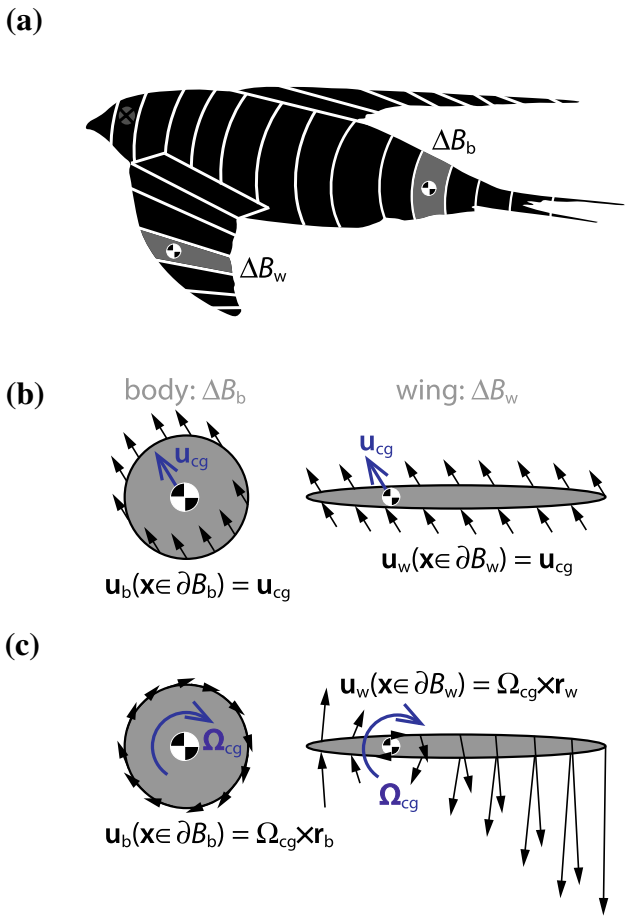

Fig. 2 A strip-theory based evaluation to determine the effect of body kinematics and shape on the unsteady body force experienced by a deforming body moving through a fluid. **a** Analogous to the blade element method, we divide the main body and lifting surfaces into thin strips, ΔB_b and ΔB_w, respectively, in which we can more easily evaluate the effect of body kinematics on the unsteady body force integral. For small body deformations, the velocity and acceleration distribution on the boundary depends on the average solid-body translational motion (**b**), and rotational motion (**c**), at the center of gravity (cg) of each element. The velocity vectors can be replaced with acceleration vectors to conduct the analysis for solid-body accelerations. Here subscripts b, w, cg, refer to the body, wing, and center of gravity, respectively, ∂B is the outer surface of the body element, **u** is the velocity, **Ω** is the angular velocity, and **r** the radial distance from the cg

This shows that the unsteady body force term acting on the body (Eqs. 5, 6) will be zero for arbitrarily shaped bodies with a constant velocity distribution regardless of ε_ρ, shape, volume, and density distribution—because the rate of change of the integrated velocity over the body is zero. This applies to measurements in wind tunnels, water tunnels, and other flow channels where the flow velocity is held constant.

For buoyant bodies with a constant volume, $\dot{V}_b = 0$, homogenous density, $\nabla\rho_b = 0$, and a dynamically deforming shape, we will first consider simple examples before generalizing to show that the instantaneous fluid-force error is zero if the net instantaneous body acceleration is zero. To make the analysis more intuitive, we consider the body volume divided into strips, analogous to the blade element method for animals and vehicles moving in fluids (Dickson et al. 2008; Leishman 2006). We first analyze the unsteady body acceleration integral (Eqs. 7, 8) over the cross-section of these slices, Fig. 2. In this analysis, we assume that each slice is sufficiently thin, and that the surface normal of the cross-sections are sufficiently aligned with the local direction of the angular acceleration vector, and sufficiently perpendicular to the local linear acceleration vector (so that cosine and sine errors can be ignored). For accelerating bodies, there exist specific combinations of linear and rotational acceleration distributions over specific body shapes that can still result in a net-zero unsteady body force. The simplest explanation is that as long as the net acceleration of the body is zero, the error in the net force measured due to ignoring the unsteady body force will be zero. Take, for example, a thin arbitrary elliptic disk (Fig. 2b, c) undergoing solid-body angular acceleration with the center of angular acceleration located at the center of area—this combined acceleration and area distribution will nullify the integral (Eqs. 12, 13) for arbitrary angular acceleration profiles in time, independent of area and volume. This is illustrated for a cylinder in Fig. 2c, and holds in general as long as the net integrated acceleration vector over the body is zero.

For a combination of linear, **a**, and angular, $\dot{\boldsymbol{\Omega}}$, solid-body acceleration, the unsteady body force integral (Eq. 8) is zero when the volume-averaged linear acceleration, $\bar{\mathbf{a}}_l$, is equal and opposite to the volume-averaged rotation based acceleration, $\bar{\mathbf{a}}_r$

$$\rho_f \frac{d}{dt} \iiint_B \mathbf{u} dV = \rho_f \iiint_B \left(\dot{\boldsymbol{\Omega}} \times \mathbf{r} + \mathbf{a}\right) dV = \rho_f V_b \left(\bar{\mathbf{a}}_r + \bar{\mathbf{a}}_l\right) = \mathbf{0} \quad \text{for} \quad \bar{\mathbf{a}}_l = -\bar{\mathbf{a}}_r. \tag{13}$$

This is illustrated by combining the ellipses of Fig. 2b, c and replacing the velocity vectors with similar acceleration vector distributions that are appropriately scaled and oriented to balance out over the elliptical cross-section. Equation 13 holds more generally, independent of the fluid density ρ_f and body volume V_b, for arbitrary body volumes in which $\bar{\mathbf{a}}_l = -\bar{\mathbf{a}}_r$, which is primarily a theoretical scenario.

To evaluate the experimental error more generally when the net body acceleration is non-zero, $\bar{\mathbf{a}}_b \neq \mathbf{0}$, it is more objective to compare the unsteady body force to the weight $\left(\rho_b V_b g\right)$ of the vehicle, animal, or object,

$$\varepsilon_a \equiv \frac{\rho_f V_b a_b}{\rho_b V_b g} = \varepsilon_\rho \cdot a_b / g, \tag{14}$$

in which a_b is the magnitude of the net body acceleration. This straightforward analysis demonstrates that the unsteady body force may not be ignored when the average body accelerations are significant $\mathcal{O}(\varepsilon_a) > \mathcal{O}(\varepsilon)$. Because we compare the error to body weight, it does not diminish for thinner bodies.

3.3 Accurate force calculation for buoyant bodies with constant volume

The net fluid force can be calculated for deforming bodies with a sufficiently constant volume without measuring the unsteady body force term using a simple correction factor—regardless of the fluid-body density ratio ε_ρ. For a constant correction factor, either the density distribution or the acceleration field of the body needs to be approximately homogenous, meaning $\nabla\rho_b = 0$ or $\nabla\ddot{x}_b = \nabla\ddot{y}_b = \nabla\ddot{z}_b = \mathbf{0}$, and $\dot{V}_b = 0$. Finally, the unsteady body force can also be calculated if the acceleration field can be determined in a simple fashion, which is typical for solid body dynamics.

To calculate the correct fluid force based on the control surface integral without the unsteady body force term, we generalize Eq. 13 for a deforming body with constant volume,

$$\rho_f \frac{d}{dt} \iiint_B \mathbf{u} dV = \rho_f V_b \bar{\mathbf{a}}_b, \tag{15}$$

in which $\bar{\mathbf{a}}_b$ is the volume-averaged body acceleration, $\bar{\mathbf{a}}_{b,V} = \iiint_B \mathbf{a}_b dV / V_b$, which acts at the center of volume of the body. If the density of the body is constant throughout the body volume, $\bar{\mathbf{a}}_{b,V}$ is equal to the mass-averaged acceleration $\bar{\mathbf{a}}_{b,m} = \iiint_B \rho_b \mathbf{a}_b dV / \iiint_B \rho_b dV$. Further, the center of volume and mass in which the respective accelerations act will overlap, forming the foundation for deriving the exact unsteady body force correction factor below. Considering it is convenient in experiments to only evaluate the control surface integral for the conservation of momentum (Eq. 5) over the outer control surface CS, we define the net associated force $\mathbf{F}_{CS}(t)$, as follows:

$$\mathbf{F}_{CS}(t) \equiv \mathbf{F}(t) + \rho \frac{d}{dt} \iint_{\partial B} \mathbf{x}(\mathbf{u} \cdot \mathbf{n}) dS, \tag{16}$$

which also gives us the equation to calculate the fluid force $\mathbf{F}(t)$ based off measuring $\mathbf{F}_{CS}(t)$ and an exact correction factor.

First, we derive the fluid-force correction factor for constant-volume bodies, $\dot{V}_b = 0$, with a constant density distribution, $\nabla\rho_b = 0$, and an arbitrary acceleration distribution. The homogenous body density is a good approximation for swimming animals, although the density would be approximated as an average, $\bar{\rho}_b = m_b / V_b$, in which m_b is the mass of the body and V_b the volume. To derive an exact correction factor that accounts for the unsteady body force in Eq. 16 without having to evaluate the integral, we rewrite Eq. 16 for $\mathbf{F}(t)$. The unsteady body force term is replaced with Eq. 15, and the resulting expression is substituted in Eq. 9, which equates it to the inertia of the body as follows:

$$\begin{aligned} \mathbf{F}(t) - \mathbf{W} = \mathbf{F}_{CS}(t) - \rho_f V_b \bar{\mathbf{a}}_b(t) - \mathbf{W} = \rho_b V_b \bar{\mathbf{a}}_b(t) \rightarrow \bar{\mathbf{a}}_b(t) \\ = \frac{\mathbf{F}_{CS}(t) - \mathbf{W}}{(\rho_b + \rho_f) V_b}. \end{aligned} \tag{17}$$

Based on the resulting expression for the average body acceleration, we now derive the constant correction factor for calculating $\mathbf{F}(t)$ based on the experimentally measured fluid force $\mathbf{F}_{CS}(t)$ as

$$\mathbf{F}(t) = \mathbf{F}_{CS}(t) - \frac{\rho_f V_b}{(\rho_b + \rho_f) V_b} (\mathbf{F}_{CS}(t) - \mathbf{W}) = (1 - \zeta_a)\mathbf{F}_{CS}(t) + \zeta_a \mathbf{W}, \tag{18}$$

in which $\zeta_a = \rho_f / (\rho_b + \rho_f)$ is the correction factor for the fluid force measured via the outer control surface, $\mathbf{F}_{CS}(t)$. For animals $(\bar{\rho}_b \approx 1000\ \mathrm{kg\ m^{-3}})$ swimming in water $(\rho_f = 1000\ \mathrm{kg\ m^{-3}})$, the correction factor is significant, $\zeta_a \approx 0.5$, and needs to be accounted for. In contrast, for animals flying in air $(\rho_f = 1.2\ \mathrm{kg\ m^{-3}})$, the correction factor is insignificant, $\zeta_a \approx 0.0012$, and can safely be neglected. We thus find that omitting the unsteady body force integral in experiments is safe for bodies that do not experience significant buoyancy; $\mathcal{O}(\varepsilon_\rho) \leqslant \mathcal{O}(\varepsilon)$. When buoyancy is significant, omitting the unsteady body force can be easily corrected for with a constant correction factor, ζ_a.

Second, we derive the fluid-force correction factor for constant-volume bodies, $\dot{V}_b = 0$, with a homogenous acceleration $\nabla\ddot{x}_b = \nabla\ddot{y}_b = \nabla\ddot{z}_b = \mathbf{0}$ and an arbitrary density distribution, typical for water vehicles. If the body density is highly variable, the volume-averaged, $\bar{\mathbf{a}}_{b,V}$, and mass-averaged, $\bar{\mathbf{a}}_{b,m}$, body accelerations will differ in general. For a homogenous acceleration, however, these average accelerations will still be identical. Therefore, we find a similar correction factor for a body with constant density as above; $\zeta_\rho = \rho_f / (\bar{\rho}_b + \rho_f)$, where $\bar{\rho}_b = \iiint_B \rho_b dV / V_b$. This requires a more careful body density distribution measurement before or after the fluid force measurements (for example, based on a CT scan of an animal or the CAD model of a vehicle).

Further, for deforming bodies with a known acceleration field in the body and an arbitrary density distribution, there still exists a straightforward calculation for the correct fluid force. For example, if the body undergoes simple combinations of linear and angular accelerations (e.g., Fig. 2b, c),

the acceleration field may be straightforward to determine experimentally. To calculate the fluid force, the volume-averaged body acceleration, $\bar{\boldsymbol{a}}_{\mathrm{b,V}}$, needs to be determined and multiplied with the body mass to correct the force measured with the outer control surface,

$$\mathbf{F}(t) = \mathbf{F}_{\mathrm{CS}}(t) - \rho_{\mathrm{f}} V_{\mathrm{b}} \bar{\mathbf{a}}_{\mathrm{b,V}}. \tag{19}$$

However, the additional measurement of volume-averaged body acceleration to calculate fluid force using Eq. 19 is generally not needed if a small error is permitted.

Finally, for most bodies experiencing buoyancy in biology and engineering, the error made by approximating the volume-averaged body acceleration, $\bar{\boldsymbol{a}}_{\mathrm{b,V}}$, with the mass-averaged body acceleration, $\bar{\boldsymbol{a}}_{\mathrm{b,m}}$, will be acceptable. The resulting error in calculating the fluid force as $\mathbf{F}(t) = \left(1 - \zeta_{\rho}\right)\mathbf{F}_{\mathrm{CS}}(t) + \zeta_{\rho}\mathbf{W}$ based on measuring $\mathbf{F}_{\mathrm{CS}}(t)$ and the weight, $\mathbf{W}$, as well as using $\zeta_{\rho} = \rho_{\mathrm{f}}/\left(\bar{\rho}_{\mathrm{b}} + \rho_{\mathrm{f}}\right)$ as a first approximation will generally be good enough. Especially, because the effect of density inhomogeneity will generally average out and the error is thus likely to reduce towards $\mathcal{O}(\varepsilon)$. If it is essential to meet strict accuracy requirements, e.g., in physics, the unsteady body force (Eqs. 7, 8) needs to be measured and included in the control surface integral whenever the density is inhomogeneous and the acceleration is complex with $\mathcal{O}\left(\varepsilon_{\mathrm{a}}\right) > \mathcal{O}(\varepsilon)$.

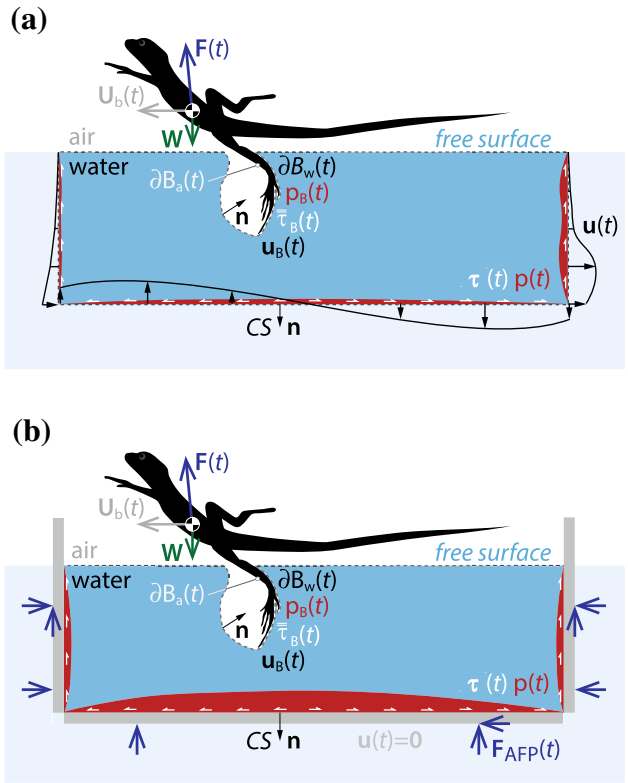

Fig. 3 Control volume analysis for measuring the fluid force generated during locomotion at the interface of water and air. The basilisk lizard cartoon is enlarged for clarity and can be replaced with any deformable body of interest that has a small contact surface with the liquid. Again, the PIV, (**a**) and AFP control surfaces, (**b**) are constructed as in Fig. 1, however, this time with a free surface that interfaces the liquid (water) and gas (air) phase. Both the PIV and AFP control surfaces are submerged in a larger volume of liquid (light blue), which is static for the AFP. Submerging the AFP in the liquid reduces the net static load on its walls from the entire weight of the control volume to just the buoyancy of the AFP walls. The basilisk cartoon has been adapted from (Hsieh and Lauder 2004)

3.4 Approximation for constant-volume bodies at the liquid–gas interface

Many water vehicles and several aquatic animals generate fluid force at the water–air interface, such as boats and the enigmatic basilisk lizard that can run over water (Hsieh and Lauder 2004), Fig. 3. For animals, vehicles and objects moving at constant velocity, the unsteady body force and the associated error will be zero as shown before (Eq. 12). Therefore, we focus here on bodies that experience significant body acceleration, as is the case for the basilisk running over water (Hsieh and Lauder 2004). The key assumption that we have to make is that most of the body area is surrounded by gas and only a small segment by liquid, as is the case for the basilisk lizard (Hsieh and Lauder 2004). The visually most apparent challenge is to evaluate the contribution of the dynamically deforming free surface at the interface, Fig. 3.

At the liquid–gas interface, the control surface integral can be simplified because of the specific boundary conditions that apply (Batchelor 2000). Due to the large density discontinuity over the interface, the stress in the gas may be considered constant and equal to $-p_0\bar{\bar{\mathbf{I}}}$ everywhere in the gas, including at the gas-side of the interface (in which $\bar{\bar{\mathbf{I}}}$ is the identity tensor). In contrast, the pressure on the liquid-side of the interface is a function of the radius of curvature of the interface via surface tension, resulting in a pressure discontinuity over a deformed interface. Further, the shear stress on the gas-side of the interface is negligible, $\bar{\bar{\boldsymbol{\tau}}} \cdot \mathbf{n} = \mathbf{0}$. Finally, there is also no-flow through the interface; $[(\mathbf{u} - \mathbf{v}) \cdot \mathbf{n}] = 0$. In concert, these boundary conditions simplify the control surface formulation for conservation of momentum (Eq. 5) as follows:

$$\begin{aligned}\mathbf{F}(t) &= -\left(\iint_{\partial B_{\mathrm{w}}} -p\mathbf{n}\mathrm{d}S + \iint_{\partial B_{\mathrm{w}}} \bar{\bar{\boldsymbol{\tau}}} \cdot \mathbf{n}\mathrm{d}S\right) \\ &= -\iint_{\mathrm{CS}} p\mathbf{n}\mathrm{d}S + \iint_{\mathrm{CS}} \bar{\bar{\boldsymbol{\tau}}} \cdot \mathbf{n}\mathrm{d}S - \rho\frac{\mathrm{d}}{\mathrm{d}t}\iint_{\mathrm{CS}} \mathbf{x}(\mathbf{u} \cdot \mathbf{n})\mathrm{d}S \\ &\quad -\rho\iint_{\mathrm{CS}} \mathbf{u}[(\mathbf{u} - \mathbf{v}) \cdot \mathbf{n}]\mathrm{d}S.\end{aligned} \tag{20}$$

This momentum balance shows how the segment of the body surface that is in contact with the water, ∂B_w, transfers the fluid force, $\mathbf{F}(t)$, to the body. The stress exerted on the air-side of the free surface, FS, and the surface segment of the body that is in contact with air, ∂B_a, can be neglected because the air pressure is constant over ∂B_a (Batchelor 2000). The air pressure, p_0, at the control surface is effectively constant and acts everywhere around the control surface (Batchelor 2000), therefore, it makes no net force contribution when integrated over the closed control surface. Further, the shear contribution of the air touching the free surface is negligible for gas–water interfaces (Batchelor 2000),

$$\iint_{\mathrm{FS}} \overline{\overline{\boldsymbol{\tau}}} \cdot \mathbf{n} \mathrm{d}S = \mathbf{0}. \tag{21}$$

Applying the no-flow condition on the interface, we also find that the momentum transfer integral over the free surface is zero,

$$-\rho \iint_{\mathrm{FS}} \mathbf{u}[(\mathbf{u}-\mathbf{v}) \cdot \mathbf{n}] \mathrm{d}S = \mathbf{0}. \tag{22}$$

If we focus on large animals and vehicles, the fluid inertia and buoyancy forces will dominate surface tension due to interface curvature. Because the associated Weber and Bond numbers will be much larger than 1 (Bush and Hu 2006), we can neglect the surface tension acting on the body at the water–air interface contact-line, $C_{\mathrm{i,b}}$, between ∂B_w and ∂B_a.

Finally, the unsteady body force (Eqs. 7, 8) can be neglected in Eq. 20 because both the mass of the air and water displaced by the body are small. For the large segment of the body volume surrounded by air, B_a, the density ratio is very small, $\varepsilon_\rho < \mathcal{O}(\varepsilon)$. Therefore, the unsteady body force associated with the mass of air displaced by the body volume, B_a, can be neglected, because the ratio of the displaced air mass and the body mass, $\varepsilon_{\mathrm{m,a}} \equiv \rho_a B_a / \rho_b V_b$, is sufficiently small; $\mathcal{O}\left(\varepsilon_{\mathrm{m,a}}\right) \leqslant \mathcal{O}(\varepsilon)$. Similarly, the unsteady body force associated with the small mass of water displaced by the body volume, B_w, can be neglected when the mass of the water displaced by the wetted body segment is small enough compared to the mass of the body $\mathcal{O}\left(\varepsilon_{\mathrm{m,w}}\right) \leqslant \mathcal{O}(\varepsilon)$, with $\varepsilon_{\mathrm{m,w}} = \rho_w B_w / \rho_b V_b$ and $V_b = B_a + B_w$. In summary, for a body that is only wetted over a small segment, the errors in the fluid force will be much smaller than the weight of the animal or vehicle,

$$\rho \frac{\mathrm{d}}{\mathrm{d}t} \iint_{\partial B} \mathbf{x}(\mathbf{u} \cdot \mathbf{n}) \mathrm{d}S = \rho \frac{\mathrm{d}}{\mathrm{d}t} \iint_{\partial B_a} \mathbf{x}(\mathbf{u} \cdot \mathbf{n}) \mathrm{d}S + \rho \frac{\mathrm{d}}{\mathrm{d}t} \iint_{\partial B_w} \mathbf{x}(\mathbf{u} \cdot \mathbf{n}) \mathrm{d}S \ll \mathbf{W}. \tag{23}$$

This approximation is particularly acceptable in animal biomechanics research, because the genetic variation between individuals and behavioral variability will typically be larger than the errors in the fluid force.

Integrating all these simplifications and adding the no-flow and no-slip boundary conditions for the mechanical control surface of the AFP in Eq. 20, we find that the fluid forces generated by animals and vehicles at liquid–gas interfaces can be measured using either PIV or the AFP (although PIV cannot establish the buoyancy contribution to fluid force). The AFP force measurement is based on the following straightforward mechanical integration of pressure and shear stress over the control surface,

$$\mathbf{F}(t) = -\left(\iint_{\partial B_w} -p\mathbf{n} \mathrm{d}S + \iint_{\partial B_w} \overline{\overline{\boldsymbol{\tau}}} \cdot \mathbf{n} \mathrm{d}S \right) = -\iint_{\mathrm{CS}} p\mathbf{n} \mathrm{d}S + \iint_{\mathrm{CS}} \overline{\overline{\boldsymbol{\tau}}} \cdot \mathbf{n} dS. \tag{24}$$

Regardless of the applicability of PIV and the AFP for measuring the fluid forces, at small Weber and Bond numbers $< \mathcal{O}(1)$, the curvature at the interface contact-line with the body needs to be measured to include surface tension (Bush and Hu 2006). Furthermore, for accelerating bodies submerged to a degree that $\mathcal{O}\left(\varepsilon_{\mathrm{m,w}}\right) > \mathcal{O}(\varepsilon)$, the unsteady body force (Eqs. 7, 8) needs to be measured and included in the control surface integral.

3.5 Variable body density and volume error

For more general bodies that experience significant buoyancy, $\mathcal{O}\left(\varepsilon_\rho\right) > \mathcal{O}(\varepsilon)$, with a density distribution and volume that change over time, we need to explicitely evaluate the effect of gravity. For this we redefined fluid pressure in Eq. 1 so that it includes the static pressure due to gravity as follows $p(t) \equiv p(t) + p_0 + \rho g H$, in which g is the gravity constant, H the depth under the (free) surface in the z direction (Fig. 1a, c), and p_0 the static pressure at zero depth, $H = 0$. In most of our fluid force derivations for gasses, the gravity term could be ignored, however, for liquids buoyancy is generally significant. Further, for all buoyant bodies of which the density and volume varies significantly over time, dynamic buoyancy effects need to be included. Pressure due to gravity is included in Eq. 3 and can be evaluated via the redefined pressure above for a general deformable control volume,

$$\iint_{\partial V} \left(\rho_f g H\right) \mathbf{n} \mathrm{d}S = \iint_{\mathrm{CS}} \left(\rho_f g H\right) \mathbf{n} \mathrm{d}S + \iint_{\partial B} \left(\rho_f g H\right) \mathbf{n} \mathrm{d}S. \tag{25}$$

Without the body present in the control volume, the first surface integral over the outer control surface represents the weight of the fluid resting on the boundaries; this static contribution can be biased to zero (tared) in AFP

measurements. When the body is added to the AFP, the first integral sums the static pressure changes on the AFP control surface due to buoyancy of the body. The second term represents the buoyancy force on the body due to the volume displaced by the body, $\partial B(t)$, equivalent to Archimedes principle (Saffman 1992), showing how the buoyancy force can be measured with the AFP. Whereas the AFP can determine the buoyancy forces on the body via the pressure field induced by the body on the outer control surface, PIV cannot, with the resulting error in the fluid force being equal to the buoyancy force. Further, the error in the measured fluid force due to buoyancy changes, as compared to body weight, depends on how much the volume of the body varies over time,

$$\varepsilon_{\Delta V} \equiv \frac{\rho_f \Delta V_b g}{\rho_b V_b g} = \varepsilon_\rho \cdot \Delta V_b / V_b. \tag{26}$$

For PIV, the body volume change, ΔV_b, must be measured carefully when $\mathcal{O}(\varepsilon_{\Delta V}) > \mathcal{O}(\varepsilon)$, regardless of the rate at which the volume changes, if the change takes place within the measurement period and is large compared to the body volume, V_b. This is relevant for fish with swim bladders and submarines, as well as balloons and zeppelins when the average volume or density of the body changes significantly.

In the case of a significant body volume rate-of-change $\mathcal{O}(V_b a_b / \dot{V}_b U_b) \leqslant 1$ (see Eq. 10), we find that larger body volumes reduce error in both PIV and AFP based fluid force measurements,

$$\varepsilon_{\dot{V}} \equiv \frac{\rho_f \dot{V}_b U_b}{\rho_b V_b a_b} = \varepsilon_\rho \cdot \frac{\dot{V}_b U_b}{V_b a_b}. \tag{27}$$

So, in general smaller and thinner volumes do not reduce fluid force error across the broad range of body kinematics and shapes considered here. Whenever $\mathcal{O}(\varepsilon_{\Delta V}) > \mathcal{O}(\varepsilon)$, buoyancy force changes need to be measured and included in PIV studies, and when $\mathcal{O}(\varepsilon_{\dot{V}}) > \mathcal{O}(\varepsilon)$, the unsteady body force (Eqs. 7, 8) needs to be measured and included in both PIV and AFP studies.

Table 1 Summary of proposed solutions for attaining accurate nonintrusive fluid-force measurements based on control-surface integration for a wide range of applications, including vehicles (*ve*), animals (*an*) and objects (*ob*)

Parameters	Sections										
	3.1	3.2	3.2	3.3	3.3	3.3	3.4	3.4	3.4	3.5	3.5
Body density ratio ε_ρ	$\leq \mathcal{O}(\varepsilon)$	$> \mathcal{O}(\varepsilon)$	$> \mathcal{O}(\varepsilon)$	$> \mathcal{O}(\varepsilon)$	$> \mathcal{O}(\varepsilon)$	$> \mathcal{O}(\varepsilon)$	$\leq \mathcal{O}(\varepsilon)$	$\leq \mathcal{O}(\varepsilon)$	$\leq \mathcal{O}(\varepsilon)$	–	–
Body acceleration ratio ε_a	–	0	$\leq \mathcal{O}(\varepsilon)$	$> \mathcal{O}(\varepsilon)$	$> \mathcal{O}(\varepsilon)$	$> \mathcal{O}(\varepsilon)$	$> \mathcal{O}(\varepsilon)$	$> \mathcal{O}(\varepsilon)$	$> \mathcal{O}(\varepsilon)$	–	–
Body volume rate $\dot{V}_b$	0	0	0	0	0	0	0	0	0	-	$> \mathcal{O}(\varepsilon)$
Body density ρ_b	–	–	–	H	IH	IH	–	–	–	–	–
Body acceleration a_b	–	–	–	IH	H	IH	–	–	–	–	–
Liquid–gas interface	No	No	No	No	No	No	Yes	Yes	Yes	No	No
Displaced water ratio $\varepsilon_{m,w}$	N/A	N/A	N/A	N/A	N/A	N/A	$\leq \mathcal{O}(\varepsilon)$	$\leq \mathcal{O}(\varepsilon)$	$\geq \mathcal{O}(\varepsilon)$	N/A	N/A
Surface tension Bo, We	N/A	N/A	N/A	N/A	N/A	N/A	$> \mathcal{O}(1)$	$< \mathcal{O}(1)$	–	N/A	N/A
Body volume change $\varepsilon_{\Delta V}$	–	$< \mathcal{O}(\varepsilon)$	$< \mathcal{O}(\varepsilon)$	$< \mathcal{O}(\varepsilon)$	$< \mathcal{O}(\varepsilon)$	–	$< \mathcal{O}(\varepsilon)$	$< \mathcal{O}(\varepsilon)$	–	$> \mathcal{O}(\varepsilon)$	–
Solution needed	No	No	No	ζ_a	$\zeta_\rho; \bar{\rho}_b$	∂B	No	$C_{i,b}$	$\partial B; C_{i,b}$	∂B	∂B
Typical applications	ve, an, ob	ve, ob	ve, ob	ve, an, ob	ve, ob	ve, ob	an, ve	an, ve	ve, an, ob	ve, an, ob	ob

The row lists parameters that govern the various errors and the columns are associated with the order in which the solution was developed in the corresponding sections. The first column (3.1) covers all forms of flight in which buoyancy can be ignored, the other columns cover more complex conditions in liquids and gases (see the associated sections for details). The maximal measurement error allowed in the nonintrusive fluid force measurement, ε_F, depends on the research domain and is set to $\mathcal{O}(\varepsilon) \leqslant 0.01$ for engineering and $\mathcal{O}(\varepsilon) \leqslant 0.1$ for biology (see main text). The legend for the parameters is as follows: –, arbitrary; N/A, not applicable; H, homogenous; IH, inhomogeneous; $\zeta_a = \rho_f/(\rho_b+\rho_f)$ use this exact correction factor for acceleration inhomogeneity; $\zeta_\rho = \rho_f/(\bar{\rho}_b + \rho_f)$, use this exact correction factor for density inhomogeneity; $\bar{\rho}_b = \iiint_B \rho_b dV/V_b$, measure the average body density such that the error in the fluid force $\mathcal{O}(\varepsilon_F) \leqslant \mathcal{O}(\varepsilon)$;$\partial B$, measure the body shape time and space resolved such that $\mathcal{O}(\varepsilon_F) \leqslant \mathcal{O}(\varepsilon)$;$C_{i,b}$ measure the water–air interface contact-line on the body such that $\mathcal{O}(\varepsilon_F) \leqslant \mathcal{O}(\varepsilon)$. The solution cell color code for the unsteady body force error is as follows: green, no error correction is needed; blue, use the exact correction factor; gray, make body surface measurements to calculate the unsteady body force. Note that the AFP can measure the (variable) buoyancy force acting on a body while PIV cannot

3.6 Unsteady body force measurement

To determine the unsteady body force for the few conditions in which it cannot be neglected or corrected for, the surface of the body needs to be measured time-resolved. However, for most applications, this additional body measurement is obsolete whenever approximating the body volume-averaged acceleration with the body mass-averaged acceleration is acceptable. When body measurements are needed, it is useful to distinguish between engineered and biological bodies. Because most vehicles have stiff body elements undergoing solid-body motion, straightforward inertial measurement unit (IMU)-based or motion-capture-based linear and rotational acceleration measurements will do—in combination with standard body surface scans. For locomoting animals, deforming vehicles, and deforming objects, the body surface needs to be measured time and space resolved. Recently, structured light techniques have been developed that can do this based on high-speed video. The 3D reconstruction of the surface can either be initiated by elaborate manual post-processing (Wolf and Konrath 2015) or can be fully automated (Deetjen et al. 2017). Structured light 3D reconstruction works by projecting a known light pattern on the surface and recording it with a high-speed camera that has been calibrated with the projector via a direct linear transformation (DLT) calibration (Wolf and Konrath 2015; Deetjen et al. 2017). Next, the surface data needs to be used to determine the velocity field on the body surface, which was recently demonstrated for the upper surface of the flapping wings of a bird by Deetjen et al. (Deetjen et al. 2017). To ensure the unsteady body force is calculated accurately after effectively differentiating surface position twice (Eq. 7), high-resolution is required in time and space, as well as smoothing techniques to minimize noise amplification. A good numerical technique for minimizing noise in the second derivative already exists (Eilers 2003), based on which accurately calculating the unsteady body force is feasible. Further, current PIV (Gemmell et al. 2015) and AFP (Hightower et al. 2017) setups already offer sufficient optical access to scan the body surface in concert. Conveniently, however, the above error analysis demonstrates that these additional efforts are unnecessary for the majority of PIV and AFP applications in gas and for the majority of applications in liquids. This can be objectively evaluated case-by-case based on the values of the non-dimensional error parameters that determine if density, ϵ_ρ, average body acceleration, ϵ_a, body volume change, $\epsilon_{\Delta V}$, and body volume rate-of-change, $\epsilon_{\dot{V}}$, errors can be neglected. Finally, if changes in the average density of the body need to be accounted for, this can be estimated using multi-view high-speed fluoroscopy (Brainerd et al. 2010).

4 Conclusions

The control-surface integration methodology used to determine the 3D force generated by freely moving bodies in fluids is generally accurate. The estimated accuracy of this nonintrusive methodology is categorized and summarized in Table 1, and applies to particle image velocimetry and aerodynamic force platform measurements on vehicles, animals, and deforming objects. The force is determined using Reynolds transport theorem for conservation of momentum over the outer control surface around the body, submerged in gas, liquid or at the liquid–gas interface, which gives the force acting on the outer control surface $\mathbf{F}_{CS}(t)$. For non-accelerating bodies, either freely moving or mounted in a test facility, the fluid force $\mathbf{F}(t) = \mathbf{F}_{CS}(t)$. The force acting on a freely moving body that accelerates is $\mathbf{F}(t) = \left(1 - \zeta_\rho\right)\mathbf{F}_{CS}(t) + \zeta_\rho \mathbf{W}$, in which the correction factor $\zeta_\rho = \rho_f / \left(\bar{\rho}_b + \rho_f\right)$ accounts for the unsteady body force due to body acceleration, $\mathbf{W}$ is the weight of the body, ρ_f is the fluid density, and $\bar{\rho}_b$ is the average body density. Consequently, the unsteady body force and associated correction factor can be safely ignored for bodies that experience negligible buoyancy compared to their weight, e.g., all flying bodies that are heavier than air. The control-surface formulation without correction factor is also accurate for heavier than air bodies that operate at the liquid–gas interface, provided the body is only submerged to a small degree, such as the legs and feet of the basilisk lizard running over water. When bodies experience significant buoyancy, however, the constant correction factor ζ_ρ is required to accurately determine the fluid force based on measuring $\mathbf{F}_{CS}(t)$, which applies to swimming animals and water vehicles in general. In contrast, when the volume of the body changes significantly, or the rate of change in body volume is significant (and in two other cases listed in Table 1), the unsteady buoyancy or body force may need to be determined by measuring the shape of the body time-resolved, and numerically evaluating Eq. 7. However, for most applications across engineering, biology, and physics, fluid force can be measured accurately without measuring the unsteady body force.

Acknowledgements I thank Rivers Ingersoll, Diana Chin, Ben Hightower, and John Dabiri for critically reading the manuscript and helpful discussion, as well as Farid Jafari for stimulating discussion. DL was supported by NSF CAREER Award 1552419.

References

Batchelor GK (2000) An introduction to fluid dynamics. Cambridge University Press, Cambridge

Brainerd EL, Baier DB, Gatesy SM, Hedrick TL, Metzger KA, Gilbert SL, Crisco JJ (2010) X-ray reconstruction of moving morphology (XROMM): precision, accuracy and applications in comparative

biomechanics research. J Exp Zool Part Ecol Genet Physiol 313:262–279
Bush JW, Hu DL (2006) Walking on water: biolocomotion at the interface. Annu Rev Fluid Mech 38:339–369
Chin DD, Lentink D (2017). How birds direct impulse to minimize the energetic cost of foraging flight. Sci Adv. 3:e1603041
Deetjen ME, Biewener AA, Lentink D (2017) High-speed surface reconstruction of a flying bird using structured light. J Exp Biol 220(11):1956–1961
DeVoria AC, Carr ZR, Ringuette MJ (2014) On calculating forces from the flow field with application to experimental volume data. J Fluid Mech 749:297–319
Dickinson MH, Lehmann F-O, Sane SP (1999) Wing rotation and the aerodynamic basis of insect flight. Science 284:1954–1960
Eilers PH (2003) A perfect smoother. Anal Chem 75:3631–3636
Gemmell BJ, Colin SP, Costello JH, Dabiri JO (2015) Suction-based propulsion as a basis for efficient animal swimming. Nat Commun 6. https://doi.org/10.1038/ncomms9790
Gutierrez E, Quinn DB, Chin DD, Lentink D (2016) Lift calculations based on accepted wake models for animal flight are inconsistent and sensitive to vortex dynamics. Bioinspir Biomim 12:16004
Hightower BJ, Ingersoll R, Chin DD, Lawhon C, Haselsteiner AF, Lentink D (2017) Design and analysis of aerodynamic force platforms for free flight studies. Bioinspiration Biomim 12(6):064001
Hsieh ST, Lauder GV (2004) Running on water: three-dimensional force generation by basilisk lizards. Proc Natl Acad Sci USA 101:16784–16788
Lentink D, Haselsteiner AF, Ingersoll R (2015) In vivo recording of aerodynamic force with an aerodynamic force platform: from drones to birds. J R Soc Interface 12:20141283
Meriam JL, Kraige LG (1993) Engineering mechanics: dynamics, vol 2, 3rd edn. Wiley, New York
Mohebbian A, Rival DE (2012) Assessment of the derivative-moment transformation method for unsteady-load estimation. Exp Fluids 53:319–330
Noca F, Shiels D, Jeon D (1999) A comparison of methods for evaluating time-dependent fluid dynamic forces on bodies, using only velocity fields and their derivatives. J Fluids Struct 13:551–578
Poelma C, Dickson WB, Dickinson MH (2006) Time-resolved reconstruction of the full velocity field around a dynamically-scaled flapping wing. Exp Fluids 41:213–225
Rae WH, Pope A (1984) Low-speed wind tunnel testing. Wiley, New York
Rival DE, Van Oudheusden B (2017) Load-estimation techniques for unsteady incompressible flows. Exp Fluids 58:20
Saffman PG (1992) Vortex dynamics. Cambridge University Press, Cambridge
Spedding GR, Hedenström A (2009) PIV-based investigations of animal flight. Exp Fluids 46:749–763
Tronchin T, David L, Farcy A (2015) Loads and pressure evaluation of the flow around a flapping wing from instantaneous 3D velocity measurements. Exp Fluids 56:7
Unal MF, Lin J-C, Rockwell D (1997) Force prediction by PIV imaging: a momentum-based approach. J Fluids Struct 11:965–971
Wolf T, Konrath R (2015) Avian wing geometry and kinematics of a free-flying barn owl in flapping flight. Exp Fluids 56:28
Wu J-Z, Pan Z-L, Lu X-Y (2005) Unsteady fluid-dynamic force solely in terms of control-surface integral. Phys Fluids 17:98102 (**1994-Present**)